



UvA-DARE (Digital Academic Repository)

Revealing viscoelastic bending relaxation dynamics of isolated semiflexible colloidal polymers

Stuij, S.G.; Jonas, H.J.; Gong, Z.; Sacanna, S.; Kodger, T.E.; Bolhuis, P.G.; Schall, P.

DOI

[10.1039/d1sm00556a](https://doi.org/10.1039/d1sm00556a)

Publication date

2021

Document Version

Final published version

Published in

Soft Matter

License

Article 25fa Dutch Copyright Act (<https://www.openaccess.nl/en/policies/open-access-in-dutch-copyright-law-taverne-amendment>)

[Link to publication](#)

Citation for published version (APA):

Stuij, S. G., Jonas, H. J., Gong, Z., Sacanna, S., Kodger, T. E., Bolhuis, P. G., & Schall, P. (2021). Revealing viscoelastic bending relaxation dynamics of isolated semiflexible colloidal polymers. *Soft Matter*, 17(36), 8291-8299. <https://doi.org/10.1039/d1sm00556a>

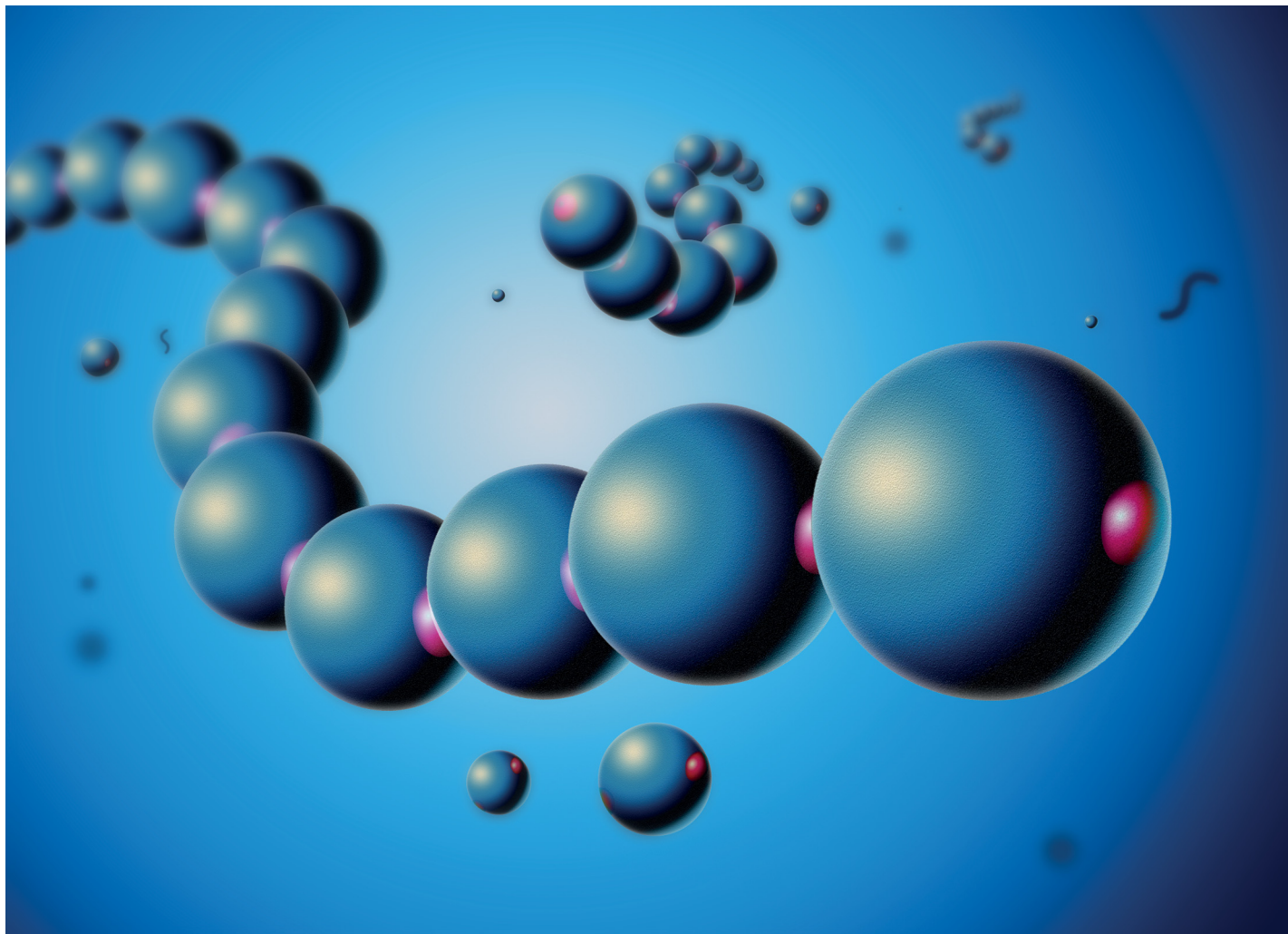
General rights

It is not permitted to download or to forward/distribute the text or part of it without the consent of the author(s) and/or copyright holder(s), other than for strictly personal, individual use, unless the work is under an open content license (like Creative Commons).

Disclaimer/Complaints regulations

If you believe that digital publication of certain material infringes any of your rights or (privacy) interests, please let the Library know, stating your reasons. In case of a legitimate complaint, the Library will make the material inaccessible and/or remove it from the website. Please Ask the Library: <https://uba.uva.nl/en/contact>, or a letter to: Library of the University of Amsterdam, Secretariat, Singel 425, 1012 WP Amsterdam, The Netherlands. You will be contacted as soon as possible.

UvA-DARE is a service provided by the library of the University of Amsterdam (<https://dare.uva.nl>)



**Highlighting research from the Soft Matter Laboratory
Amsterdam, from the group of Prof. Peter Schall.**

Revealing viscoelastic bending relaxation dynamics of
isolated semiflexible colloidal polymers

Semiflexible colloidal polymers made from di-patch colloidal particles, exhibiting bending fluctuations and relaxation. Immersed in a near-critical binary liquid, the particle patches interact *via* critical Casimir forces. We experimentally study and theoretically model the thermally activated bending modes of individual colloidal polymers. Our results reveal viscoelastic relaxation dynamics with bending rigidity and internal friction tuneable by the patch-patch interaction. (Artist impression: Madison Arias)

As featured in:



See Simon G. Stuij, Peter Schall *et al.*,
Soft Matter, 2021, 17, 8291.



Cite this: *Soft Matter*, 2021,
17, 8291

Revealing viscoelastic bending relaxation dynamics of isolated semiflexible colloidal polymers†

Simon G. Stuij, ^{*a} Hannah J. Jonas, ^b Zhe Gong, ^c Stefano Sacanna, ^c
Thomas E. Kodger, ^d Peter G. Bolhuis ^b and Peter Schall ^{*a}

The viscoelastic properties of filaments and biopolymers play a crucial role in soft and biological materials from biopolymer networks to novel synthetic metamaterials. Colloidal particles with specific valency allow mimicking polymers and more complex molecular structures at the colloidal scale, offering direct observation of their internal degrees of freedom. Here, we elucidate the time-dependent viscoelastic response in the bending of isolated semi-flexible colloidal polymers, assembled from dipatch colloidal particles by reversible critical Casimir forces. By tuning the patch–patch interaction strength, we adjust the polymers’ viscoelastic properties, and follow spontaneous bending modes and their relaxation directly on the particle level. We find that the elastic response is well described by that of a semiflexible rod with persistence length of order 1000 μm , tunable by the critical Casimir interaction strength. We identify the viscous relaxation on longer timescales to be due to internal friction, leading to a wavelength-independent relaxation time similar to single biopolymers, but in the colloidal case arising from the contact mechanics of the bonded patches. These tunable mechanical properties of assembled colloidal filaments open the door to “colloidal architectures”, rationally designed (network) structures with desired topology and mechanical properties.

Received 15th April 2021,
Accepted 23rd July 2021

DOI: 10.1039/d1sm00556a

rsc.li/soft-matter-journal

I Introduction

The mechanical properties of filaments and biopolymers are central to many soft and biological materials, crucially determining their function. They are important in the packaging and replication of DNA,¹ the swimming behavior of bacteria,^{2–4} and the mechanics of assembled (bio)polymer networks.⁵ In contrast to flexible synthetic polymers such as polybutadiene, biopolymers are often semiflexible and have a finite bending rigidity, which describes the elastic restoring force to bending deformations. In biopolymer networks, bending deformations allow stabilization of the network below the isostatic limit, and can couple to stretching modes of the fibres.^{6,7} This is also the case for elastic networks, where the bending rigidity can significantly stiffen the network,⁸ and for colloidal gels.⁹ The bending rigidity plays also an

important role in the viscoelastic properties of dense solutions of semiflexible polymers, where also tension along the chains and entanglements comes into play,¹⁰ as experimentally visualized for actin filaments,¹¹ as well as in self-assembly processes, where the bending influences the dynamic formation path and affects the final structural stability.¹² When coupled with activity, it can have interesting dynamic effects: flexible chains diffuse markedly faster compared to their stiff counterparts,¹³ and activity coupled with semiflexible chains of appropriate bending rigidity leads to interesting steady-state oscillations of the filament, imitating that of periodically moving biological filaments such as cilia.¹⁴

While already simple aggregated colloids can exhibit rigid bonds leading to bending rigidity,^{15–17} recent realization of anisotropic “patchy” interactions^{18–29} opens new opportunities for assembling and investigating colloidal analogs of filaments and simple biopolymers: the particle patches set the local valence and bond angles, causing the formation of geometrically distinct structures such as straight chains, cyclic structures and networks. With this new level of control, we can now address key questions about the mechanical properties of such assemblies, and how to tune these mechanical properties with experimentally available control parameters. As particles with directed interactions form open structures with pre-set connectivity, we expect interesting, tunable viscoelastic

^a Institute of Physics, University of Amsterdam, Science Park 904, 1098 XH Amsterdam, The Netherlands. E-mail: s.g.stuij@uva.nl, p.schall@uva.nl

^b van't Hoff Institute for Molecular Sciences, University of Amsterdam, Science Park 904, 1098 XH Amsterdam, The Netherlands

^c Molecular Design Institute, Department of Chemistry, New York University, 29 Washington Place, New York 10003, USA

^d Physical Chemistry and Soft Matter, Wageningen University, Stippeneng 4, 6708 WE Wageningen, The Netherlands

† Electronic supplementary information (ESI) available. See DOI: 10.1039/d1sm00556a

properties to emerge that can be tailored by the building blocks and their mutual interactions.

In particular, the application of critical Casimir forces on patchy particles allows tunable patch–patch interactions to be realized.^{30,31} The attractive interaction arises from the confinement of fluctuations of a near-critical solvent between the surface-modified patches, and allows reversible control over their attractive strength via the temperature offset from the solvent critical temperature, T_c ,^{32–37} providing genuine control of the colloidal phase^{38–40} and gelation behavior.^{41–43} Specifically, using divalent particles, analogues of polymers form that, in equilibrium, show the expected exponential length distributions in agreement with Flory theory predictions.^{28,31} These colloidal polymers provide simple, directly observable models of their molecular and biological counterpart.

In this paper, we explore the viscoelastic bending response of patchy-particle chains, colloidal analogues of semiflexible polymers, assembled from di-patch colloidal particles. We employ critical Casimir interactions to tune the strength of the patch–patch bond *in situ*, and measure its effect on the viscoelastic properties of the chain. By analyzing the bending mode spectrum and its dynamic evolution, we find that on short timescales, the dipatch particle chain is well described as a semiflexible elastic filament, with attraction-dependent bending rigidity. On longer timescales, bending fluctuations relax in a two-step process, which we associate with external fluid drag and internal friction due to slow conformational changes. The viscoelastic response reflects that of biological filaments,^{44,45} exhibiting similar wave-length independent internal friction, which in our case we associate with the surface friction arising at the particle-scale contact. These results demonstrate mechanical control of assembled colloidal polymers and more complex molecule-like structures, suggesting the future design of colloidal superstructures with mechanical properties that can be tuned by the experimentalist. We envisage that programmatic control over the bending rigidity, especially in low-coordinated network structures, could dramatically shift the material response from rigid to floppy or from bending dominated to stretching dominated.^{46–48}

II Methods

We use colloidal dipatch particles consisting of a sphere with two opposing fluorescently labeled patches, prepared by a recently published colloidal fusion technique.¹⁸ Particles with two different patch sizes are used, “large-patch” particles with an average radius of $r_A = 1.6 \mu\text{m}$ with polydispersity ($\sigma(r_A)/\langle r_A \rangle$) of 3%, a patch size $\theta_{p,A} = 21^\circ(\pm 2)$ and a patch radius of curvature $R_{p,A} = 1.0(2) \mu\text{m}$, and “small-patch” particles, with an average radius of $r_B = 1.55 \mu\text{m}$ with the same polydispersity, a patch size of $\theta_{p,B} = 14^\circ(\pm 2)$ and a patch radius of curvature $R_{p,B} = 1.2(2) \mu\text{m}$. Here, the patch arc angle is defined by $\theta_{p,A} = 2 \sin^{-1}(d_{p,A}/2r_A)$, with $d_{p,A}$ the patch diameter of particle A, as measured by atomic force microscopy, and similar for particle B. The particles are dispersed in a binary mixture of

water and lutidine with lutidine volume fraction $c_L = 25\%$. Salt (0.375 mM Magnesium sulfate) is added to screen the particle charges (Debye screening length $\lambda_D = 4.5 \text{ nm}$) and increase the lutidine adsorption preference of the patches with respect to that of the particle bulk. The lutidine and salt concentrations are optimized to obtain selective patch–patch attraction in a large temperature window $\Delta T = T_{\text{cx}} - T$ below the solvent phase separation temperature $T_{\text{cx}} = 33.75 \text{ }^\circ\text{C}$. Since the density of the particles ($\rho_p \approx 1.05 \text{ g ml}^{-1}$) is larger than that of the solvent mixture ($\rho_s = 0.981 \text{ g ml}^{-1}$), the particles sediment to the bottom of the capillary, forming a quasi two-dimensional layer with gravitational height $h_A = 0.35 \mu\text{m}$ (large-patch particles) and $h_B = 0.4 \mu\text{m}$ (small-patch particles). The particle volume fraction is chosen such that after sedimentation, sufficiently long chains can form, yet their steric interaction remains small.

To form dipatch-particle chains, we heat the sedimented suspension to temperatures in a range of $\Delta T = 0.2$ to 0.05 K below T_{cx} , with a smaller ΔT causing larger interaction strength. Fine temperature control is achieved using an objective collar and sample heater coupled to a single water bath with a setting accuracy of 0.01 K . To investigate the effect of patch–patch attractive strength on the bending rigidity, we vary the temperature in steps of 0.02 K from $\Delta T = 0.19$ to $\Delta T = 0.05 \text{ K}$, waiting at least 10 minutes at each temperature before acquiring images to ensure thermal and mechanical equilibration. We then image chain conformations by acquiring optical bright-field images at a frame rate of 2 s^{-1} over a time of 30 minutes, resulting in 3600 images at each temperature. These images capture chains of different length, containing up to $N = 15$ particles. To check for reversibility, we also decrease the temperature back to $\Delta T = 0.19 \text{ K}$ using the same temperature steps; at $\Delta T = 0.17 \text{ K}$, some bonds of the chains break, and at $\Delta T = 0.19 \text{ K}$ all bonds disintegrate attesting the reversibility of the critical Casimir interaction. We locate particle centers in the recorded plane with an accuracy of 20 nm using particle-tracking software.⁴⁹ The accuracy is estimated based on the image pixel size of 103 nm and a conservative subpixel accuracy factor of 5.

We note that due to their proximity to the wall, the particles exhibit dynamics that are slowed down with respect to bulk particles due to hydrodynamic effects.⁵⁰ We therefore measured the single-particle diffusion coefficient of sedimented particles at $\Delta T = 2 \text{ K}$, where critical Casimir forces are negligible. The mean-square displacement of the large-patch particles shows a diffusive power law with diffusion coefficient $D = 0.035 \pm 0.005 \mu\text{m}^2 \text{ s}^{-1}$ (see ESI[†]), roughly half of the bulk value $D_{\text{Einstein}} = kT/6\pi r_A \eta = 0.074 \mu\text{m}^2 \text{ s}^{-1}$, where we have used the solvent viscosity $\eta = 1.9 \text{ mPa s}$ for the binary mixture at $T = 30 \text{ }^\circ\text{C}$.⁵¹ This slowdown by a factor of two is in reasonable agreement with the theoretical estimates in ref. 50

III Results and discussion

A Static analysis: single bond level

The assembled chains exhibit widely different lengths (Fig. 1(a)), following an exponential size distribution in agreement with Flory-theory predictions.³¹ Within the chains, the

particles are bonded *via* their patches, as clearly seen in the epifluorescence image highlighting the fluorescent patches in Fig. 1(b). The chains are straight on average and exhibit thermally excited bending fluctuations around this average. The amplitude of these fluctuations increases with temperature offset ΔT from T_{cs} , until the chains finally break, as shown in Fig. 1(c). These qualitative observations suggest that we can tune the bending rigidity of the chains *via* the temperature-sensitive critical Casimir force.

To explore this dependence quantitatively, we determine the effective bending angle θ_i of a dipatch particle i from the bond angles ϕ_i and ϕ_{i+1} with its neighbors according to $\theta_i = \phi_{i+1} - \phi_i$, as illustrated in Fig. 2(a and b). Time traces of θ_i for all particles within the chain are shown in Fig. 2(c and d). Indeed, they fluctuate around zero, as can be best seen by the density profiles of three selected angles in Fig. 2(e). To measure the fluctuation magnitude, we fit Gaussian distributions to the density profiles and extract their standard deviations $\sigma(\theta_i)$. Interestingly, this standard deviation varies slightly from particle to particle, indicating some inhomogeneity; to obtain a mean fluctuation measure for the whole chain, we average over all particles to obtain an average angle and show the resulting distribution of bending angles for different temperatures in Fig. 2(f). A systematic broadening of the distribution is observed with increasing ΔT corresponding to decreasing critical Casimir attraction. All angle distributions are well fitted by Gaussians; the extracted standard deviations $\langle \sigma(\theta_i) \rangle$ show an almost linear increase with temperature (Fig. 2(g)). Furthermore, the dependence is reversible: we find the same value of $\langle \sigma(\theta_i) \rangle$ upon decreasing the temperature. We thus conclude that, within accuracy, there is no hysteresis or aging of the bonds. This is in contrast to interactions between DNA-grafted colloids, which often show effects of hysteresis.⁵² Note that these measured variances are well above those related to locating uncertainty; the bond angle uncertainty corresponding to the positional uncertainty of $\varepsilon = 20$ nm is $\varepsilon_\theta = 3\varepsilon/d \approx 0.025$ rad, which further narrows down by the averaging. Thus, these bond bending variances represent true movement of the particles.

Local bending angle variances along all particles of the chain are shown in Fig. 2(h). Interestingly, the difference in fluctuation magnitude between particles persists over the different temperatures; bonds that are most flexible at one temperature are also most flexible at another, suggesting that this variation is characteristic of the chain and constituting particles. We hypothesize that to a large part this variation can be attributed to polydispersity of the patches, especially those variations that are non-monotonic along the chain. Based on atomic force microscopy measurements, we determine the patch size polydispersity to be on the order of 10% (see ESI[†]), giving rise to variation of the bond rigidity from particle to particle. Another source of variation can be standing waves on the chain. Such vibrational modes have specific position-dependent amplitudes along the chain that would result in continuous changes of bending variation along the chain. For instance, the lowest energy mode is a half sine wave with maximum bending amplitude in the middle of the chain. Looking at Fig. 2(h), the bending amplitude is indeed higher in the middle of the chain than towards the ends, in agreement with this expectation.

B Static analysis: modes and bending rigidity

To study the vibrational modes in more detail, we decompose the thermally excited bending fluctuations into Fourier modes.^{45,53} We express the bond angles as

$$\phi_i = \sqrt{\frac{2}{L_0}} \sum_{n=0}^{N-2} \alpha_q \cos(q_n s_i), \quad i \in 1, \dots, N-1, \quad (1)$$

where n is the mode number and α_q the amplitude of the n -th mode. The corresponding wave vector is defined as $q_n = n\pi/L_0$, where L_0 is the contour length of the chain and $s_i = (i-1/2)2r$ the discrete arclength along the chain, with $2r = L_0/(N-1)$ the average particle diameter. Time traces of the amplitudes of each mode are shown in Fig. 3a. Again, the distributions are centered around the $y = 0$ axis, confirming the low intrinsic

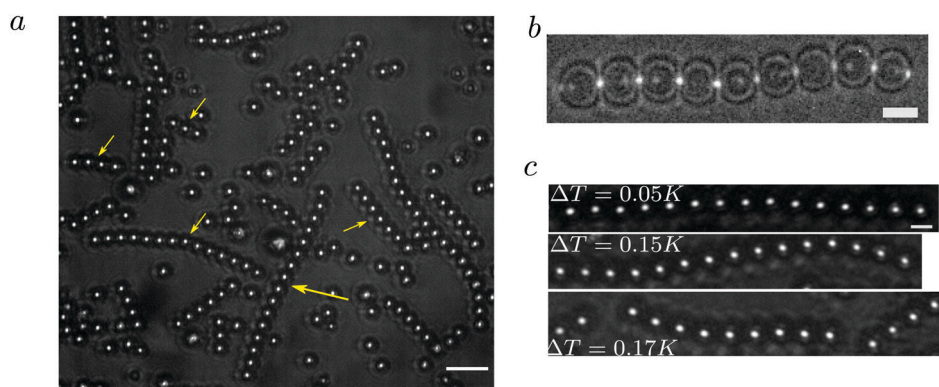


Fig. 1 Temperature-dependent fluctuations of assembled dipatch-particle chains. (a) Aggregated chains at $\Delta T = 0.1 \pm 0.01$ K, scale bar $10 \mu\text{m}$. Yellow arrows indicate some of the chains used in the analysis. (b) Epifluorescence image overlaid on a bright field microscopy image showing that the particles are bonded *via* their labeled fluorescent patches. Scale bar $3 \mu\text{m}$. (c) Bright-field images of a fluctuating colloidal chain at increasing ΔT . Bending fluctuations grow with increasing ΔT , until the chain finally breaks at $\Delta T = 0.17$ K. The focus was set slightly below conventional bright-field focusing to obtain a bright particle center for good locating accuracy of the particles. Scale bar is $3 \mu\text{m}$.

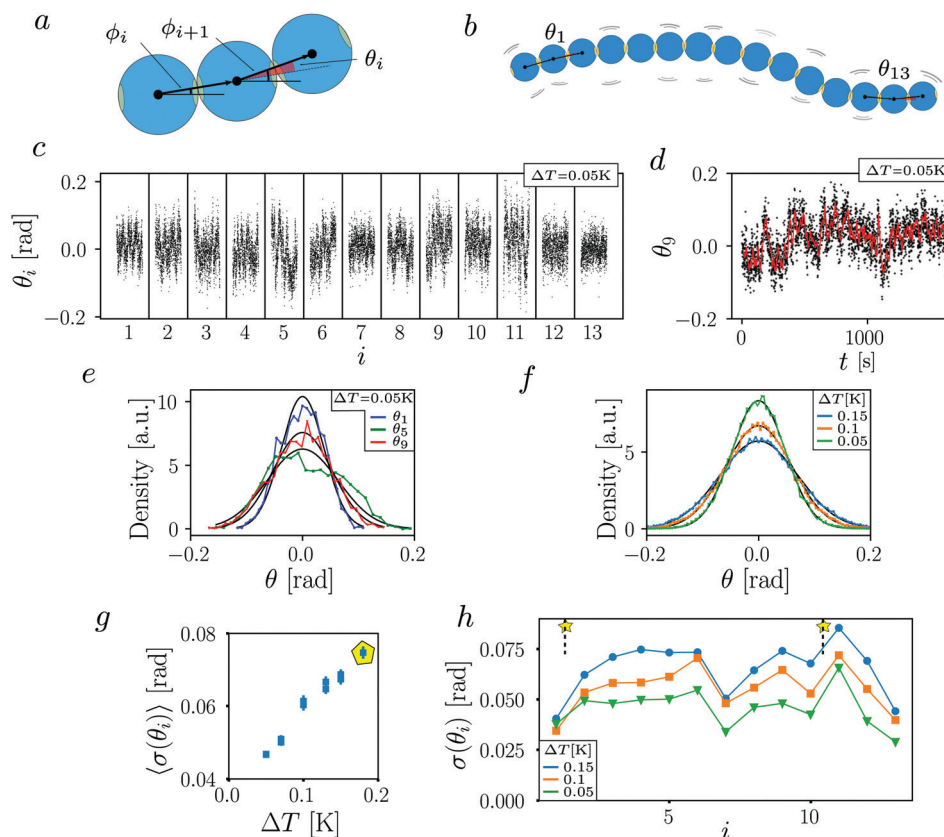


Fig. 2 Analysis of bending angles. (a and b) Definition of the tangent angle ϕ_i and bending angle θ_i . (c) Time traces of each bending angle at $\Delta T = 0.05$ measured at a frame rate of 2 s^{-1} over a 30 min time interval. (d) Zoom-in of one representative bending angle θ_9 , red line is a rolling mean over a 10 s time interval. (e) Density plot of three bending angles at a single temperature $\Delta T = 0.05$. Black lines are Gaussian fits. (f) Density plot of the average of all bending angles of the chain for three different temperatures, and Gaussian fits (black lines) (g) Average standard deviation $\langle \sigma(\theta_i) \rangle$ obtained from the Gaussian fits of the average bending angle (panel (f)) as a function of ΔT . Each point corresponds to a 30 minute measurement, error bars represent variation in σ along the chain. The yellow pentagon indicates the breaking temperature. (h) Standard deviations $\sigma(\theta_i)$ of the individual bending angles of particles i at three temperatures. Stars indicate the positions of chain breaking at $\Delta T = 0.17$ K. All data correspond to the chain depicted in Fig. 1c.

curvature of the chain. To determine the bending rigidity, we consider the worm-like chain Hamiltonian given by

$$U = \frac{B}{2} \int_0^{L_0} \left(\frac{\partial \phi}{\partial s} \right)^2 ds, \quad (2)$$

where $B = k_B T L_p$ is the bending rigidity, and L_p the persistence length. The worm-like chain model assumes a continuous filament. The tangent angle can be expressed in terms of Fourier modes as $\phi(s) = \sqrt{\frac{2}{L_0}} \sum_{n=0}^{\infty} \alpha_q^{\text{WL}} \cos(q_n s)$, with α_q^{WL} the mode amplitudes of the worm-like chain, to be distinguished from the experimental mode amplitude α_q . By inserting the Fourier decomposition into eqn (2) and assuming that every mode is excited on average with the same thermal energy $k_B T$ (equipartition theorem), it follows that the amplitude variance of a mode with wave number q is given by

$$\sigma^2(\alpha_q^{\text{WL}}) = \frac{k_B T}{B q^2} \quad (3)$$

To test this prediction, in Fig. 3b, we plot the mode amplitude variance as a function of q . Indeed, over an extended range of intermediate q , the measured variance decreases with q in a

power-law with slope -2 for all three temperatures, validating the mapping of the chain to a filament. Some deviation is observed for large q , for which the short wavelength approaches the particle scale and the continuous worm-like chain model breaks down. Some deviation also occurs for small q , possibly due to the long relaxation time of these long-wavelength modes, which becomes of the order of the measurement time. We note that while the short wavelengths are also more susceptible to noise, we remain safely above the estimated noise level for all q values.

We now determine the persistence length from a linear fit of σ^2 versus q^{-2} over the intermediate q interval, where eqn (3) applies. The resulting values (Fig. 3c) show a clear decrease with increasing ΔT , from $L_p \sim 1500 \mu\text{m}$ to $L_p \sim 500 \mu\text{m}$, corresponding to $L_p/d \sim 470$ and $L_p/d \sim 160$, respectively, showing that these chains are in the semi-flexible regime, with a finite persistence length that is significantly longer than the particle diameter. We confirm that the measured persistence length is robust for chain lengths down to $N = 10$ (Fig. 3d); for shorter chains, the continuum description breaks down and the persistence length becomes unreliable. Remarkably, the chain persistence length scales roughly linearly with the

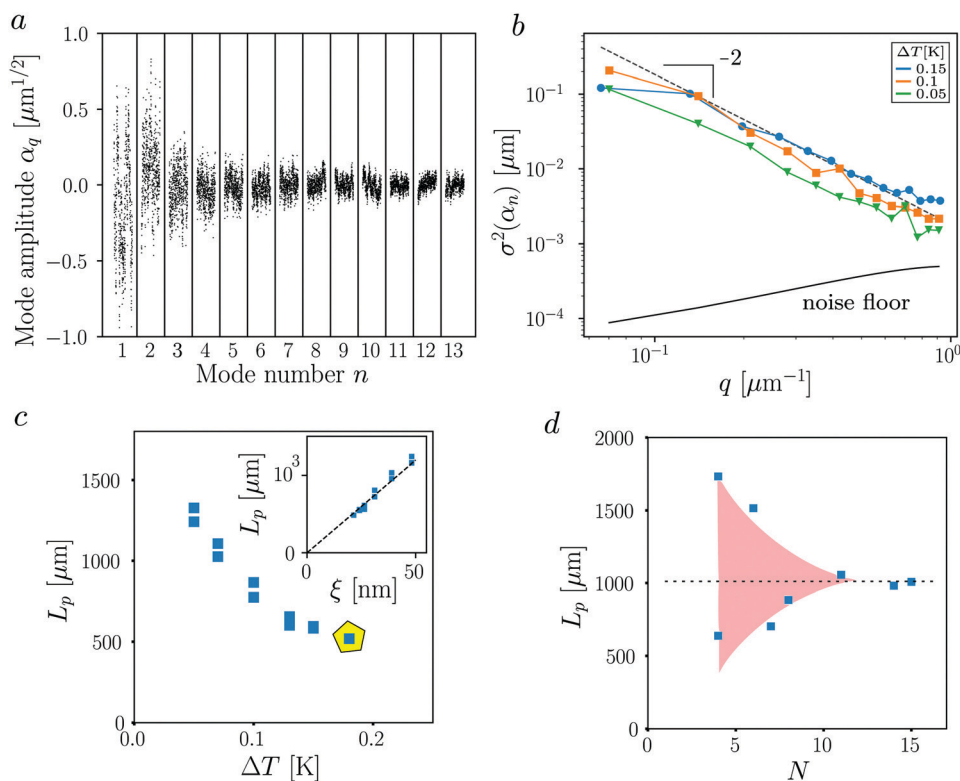


Fig. 3 Analysis of bending modes and bending rigidity. (a) Time traces of the amplitude of mode $n = 1$ to 13 at $\Delta T = 0.05$ K. (b) Variance of mode amplitude as a function of q for three different temperatures. Dashed line is a q^{-2} fit for q -values between 0.1 and 0.6 at $\Delta T = 0.15$. Indicated noise floor is based on the tracking accuracy of 20 nm. (c) Fitted persistence length versus ΔT , the yellow pentagon indicates the breaking temperature. Inset shows L_p versus $\xi = \xi_0(\Delta T/T_c)^{-0.63}$, with $\xi_0 = 0.19$ nm. Dashed line is a linear fit of L_p versus ξ . (d) Persistence length L_p versus chain size N at $\Delta T = 0.1$ K. Red area and dotted line are guides to the eye. All data in (a–c) correspond to the chain in Fig. 1c.

correlation length $\xi = \xi_0(\Delta T/T_c)^{-0.63}$ (Fig. 3c inset), estimated for a solvent at the critical composition, which is close to the correlation length of our off-critical solvent, albeit slightly larger.³⁷ Thus, changes at the smallest (solvent fluctuation) length scale affect the emergent mechanical properties on a much larger length scale.

C Dynamic analysis: two relaxation timescales

To elucidate the nature of the bending modes, we studied their dynamic evolution. An elastic filament in a solvent subject to fluctuations should show a characteristic time dependence: just like a single Brownian particle exhibiting an increasing mean-square displacement, the modes of an elastic filament exhibit increasing mean-square amplitudes, which due to the elastic restoring force, however saturate at a final steady-state value, the static variance $\sigma^2(\alpha_q)$. The full time evolution is described by the Langevin equation⁴⁵

$$B \frac{\partial^4 u}{\partial s^4} + \gamma \frac{\partial u}{\partial t} = f(s, t), \quad (4)$$

where $u(s, t)$ is the transverse position related to the tangent angle $\phi = \partial u / \partial s$, f a random thermal noise and γ is the drag coefficient per unit length of the filament. Assuming that the Fourier modes act as normal modes, which has been shown to be a valid assumption for semiflexible biopolymers,⁴⁵ eqn (4)

predicts that the time evolution of the modes' mean-square amplitudes, $\langle (\alpha_q(t + \Delta t) - \alpha_q(t))^2 \rangle_t$, to the final static variance follows a single exponential given by⁴⁵:

$$\frac{1}{2} \langle (\alpha_q(t + \Delta t) - \alpha_q(t))^2 \rangle_t = (1 - e^{-\Delta t/\tau}) \sigma^2(\alpha_q), \quad (5)$$

where the relaxation time τ is related to the drag coefficient γ and bending rigidity B by

$$\tau \simeq \frac{\gamma}{Bq_*^4}, \quad (6)$$

with $q_* \approx (n + 1/2)\pi/L_0$.

To test these predictions, we monitor the mode amplitudes over time and determine, for each mode, the mean-square amplitude as a function of lag time, which we show for mode 1 to 11 in Fig. 4(a). The data shows indeed characteristic relaxations to plateaus; interestingly, however, we observe two different relaxation timescales. This is clearly visible in the higher-order modes $n > 3$: an initial exponential relaxation towards a plateau is followed by a second relaxation. The initial exponential relaxation indicates an elastic process. We separate it from the second by performing a least-square fit of the fast relaxation with a linear weighting favoring small Δt , see Fig. 4(a), blue lines. The initial fast relaxation time follows a q_*^{-4} dependence from the second mode up to the minimal lag time set by the experimental acquisition rate (Fig. 4(b)), in line

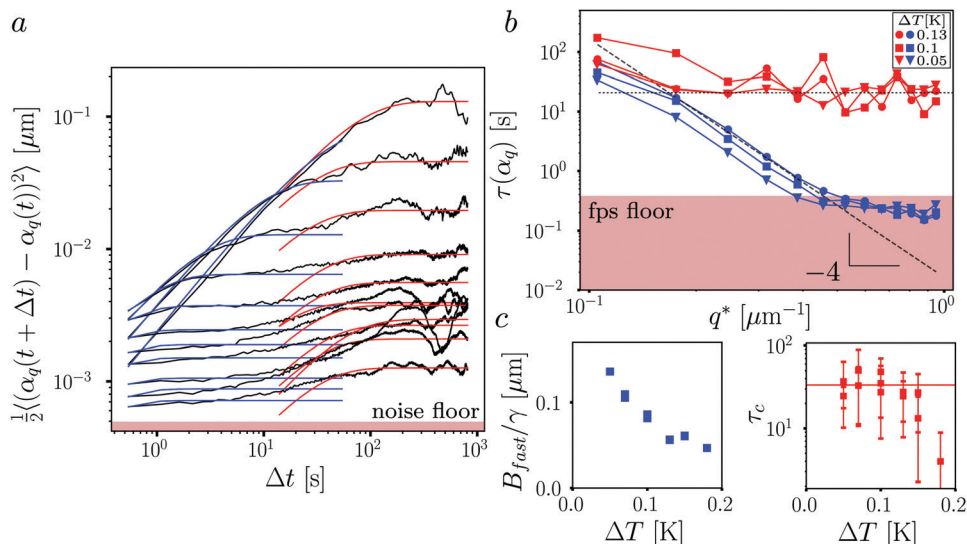


Fig. 4 Dynamic analysis of modes: two relaxation timescales. (a) Mean-square amplitude versus lag time for modes $n = 1$ to 11 (top to bottom) at $\Delta T = 0.05$ K. Blue (red) lines are exponential relaxation fits to the fast (slow) relaxation processes. (b) Fitted relaxation times τ_{fast} (blue) and τ_{slow} (red) versus q^* for three different temperatures. Dashed slope corresponds to q^*^{-4} fit of τ_{fast} at $\Delta T = 0.13$ K. Dotted line corresponds to τ_c , the constant saturation value of τ_{slow} at $\Delta T = 0.13$ K. Red lower shading corresponds to the minimum experimentally accessible $\Delta t = 0.5$ s between frames. (c, left) Temperature dependence of the bending rigidity of the fast component and drag coefficient from power-law fit. (c, right) Temperature dependence of the saturation values τ_c of τ_{slow} , determined from averaging τ_{slow} for $q^* > 0.2 \mu\text{m}^{-1}$. Error bars are the standard deviation of those values. The multiple datapoints at single temperatures correspond to multiple independent measurements at that temperature.

with eqn (6), further confirming the elastic nature of the relaxation process. Using this equation, we can then determine the ratio of bending rigidity to drag coefficient, B_{fast}/γ , as shown in Fig. 4(c) (left panel), which decreases with ΔT , as expected for the lower elastic restoring force associated with the lower critical Casimir attraction.

In contrast, the second relaxation is not well captured by an exponential. We can still determine a relaxation time by imposing an exponential fit (but with an opposite weighting as before, see red lines), and find that this second slow relaxation time does not decay with q , but tends to a constant, τ_c (Fig. 4(b)), further confirming its non-elastic origin. This constant is

shown as a function of ΔT in Fig. 4(c) (right panel); except for a lower value at lowest interaction strength, the large error bars don't allow to see a clear trend with ΔT , and we average over all points with $\Delta T < 0.17$, to obtain $\langle \tau_c \rangle = 30 \pm 10$ s.

We use this decomposition to extract the elastic component of the vibrational modes alone. To do this, we separate the mode variances $\sigma_{\text{fast}}^2(\alpha_q)$ and $\sigma_{\text{slow}}^2(\alpha_q)$, from the plateaus after the first and second relaxation times. Plotting σ_{fast}^2 as a function of q (Fig. 5(a)), we recover a remarkably clean signal for the higher q values, with a clear monotonic temperature dependence, and the expected q^{-2} dependence over an extended q range. The extracted elastic persistence lengths

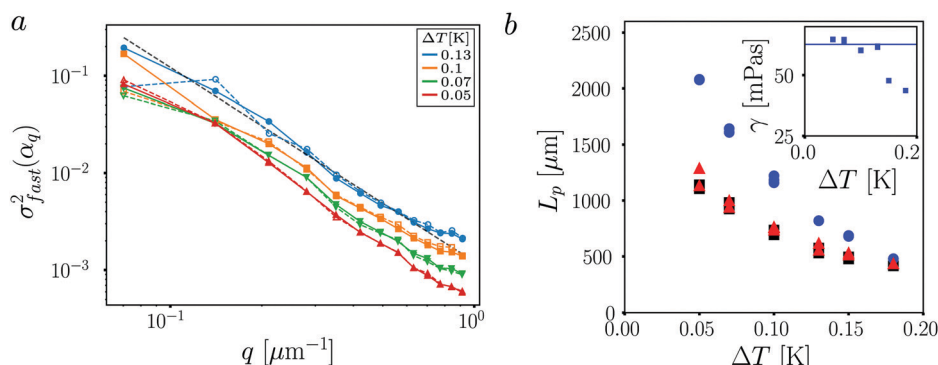


Fig. 5 Elastic mode fluctuations at short timescales (a) variance σ_{fast}^2 , extracted from the fast exponential relaxation, versus q for four different temperatures. Open/closed markers and dashed/solid lines correspond to two independent measurements, going up and down the temperature ramp, respectively. (b) Persistence length L_p obtained by fitting a q^{-2} dependence to σ_{fast}^2 , σ_{slow}^2 , and σ_{static}^2 (blue dots, red triangles, and black squares, respectively). Inset: Transverse drag coefficient per unit length, γ , determined by dividing B_{fast} by the data from Fig. 4(c). Line corresponds to the mean of γ for $\Delta T \leq 0.13$ K.

are about a factor of two higher than those extracted from the slow relaxation and obtained through the static analysis, as shown in Fig. 5(b). We use the corresponding elastic bending rigidity B_{fast} to calculate the drag coefficient γ from their previously determined ratio, see Fig. 5(b), inset. This drag coefficient remains constant for the most reliable low ΔT , for which the strongest elastic response is expected. The average value $\gamma = 63 \pm 2$ mPas is of the order of the measured drag coefficient of the transverse diffusion of the chain, $\gamma^T = 31 \pm 3$ mPa s (see ESI†), albeit a factor of two larger, possibly due to the additional rotational drag the colloidal particles experience upon chain bending.

From this we conclude that on sufficiently short timescales ($t < \tau_c$), the chain is described by an overdamped elastic process. This elastic behavior can be captured by a single elastic bending modulus B_{fast} , and drag coefficient γ , with the former largely tunable by temperature. On longer timescales, a second non-elastic relaxation process occurs. The non-exponential relaxation and wavelength-independent relaxation time, τ_c , show that this is not a standard overdamped elastic process. Such constant relaxation times have been observed before in microtubules,^{44,45,54} and attributed to extra energy losses from internal friction. In this case, the Langevin equation becomes modified by an additional dissipatory term with internal friction coefficient γ' (see ESI†), which relates to the relaxation time according to the modified equation

$$\tau = \frac{\gamma + \gamma' q_*^4}{Bq_*^4}. \quad (7)$$

The internal friction coefficient γ' can be associated with an effective internal viscosity *via* $\eta' = \gamma'/a^4$, where a is the filament diameter. Using the measured values of τ_c together with the bending rigidities $B = B_{\text{static}}$ from the static analysis, we obtain an internal friction coefficient of $\gamma' \sim 10^5$ mPa s μm^4 and an internal viscosity of $\eta' \sim 10^3$ mPa s. Furthermore, using for γ the value determined from the fast relaxation we obtain a critical wave vector of $q_c \sim 0.2 \mu\text{m}^{-1}$, above which bending relaxation is dominated by internal friction.

Interestingly, already a single bending angle (made up of three bonded particles) shows very similar slow-relaxation dynamics, see ESI.† This suggests that the slow relaxation does not originate from a collective effect, but rather arises on the single-bond level. We hence associate τ_c with friction in the patch–patch contact of two bonded particles. We speculate that the origin of this internal friction is a stick-slip like process in which the point of contact between the two colloids moves on timescales larger than τ_c ; below this timescale, the point of contact is essentially fixed giving rise to an elastic bending constant B_{fast} , while beyond this time, the contact can diffuse, still being bounded by the finite patch size. This is also in line with previous observations of the plastic buckling of chains.¹⁷ With decreasing particle size, τ_c likely decreases as thermal agitation more easily overcomes contact–contact friction for smaller particles.

D Dependence on patch size

We finally investigated the influence of patch size by using dipatch particles with significantly smaller patches, and otherwise identical properties, see ESI.† Their patch arc angle is $\theta_{\text{p,B}} = 14^\circ(\pm 2)$ instead of $\theta_{\text{p,A}} = 21^\circ(\pm 2)$, hence two thirds of the patch size of the previously investigated particles. By full dynamic analysis of the modes, we find a very similar relaxation behavior: a robust two-step relaxation process with similar dependence of plateaus and relaxation time on q and q_* . Interestingly, the corresponding persistence lengths of the fast and slow relaxations are both a factor of ~ 2 higher than those of the larger-patch particles. The higher persistence length of the slow relaxation is qualitatively expected from the more restricted range of bond angles for smaller patch sizes. The higher persistence length of the fast relaxation is surprising as one naively expects a smaller patch to exhibit lower interaction strength. However, while the size of the patch is smaller, its radius of curvature is bigger: $R_{\text{p,B}} = 1.2(2) \mu\text{m}$ instead of $R_{\text{p,A}} = 1.0(2) \mu\text{m}$. Consequently, the patches are flatter, resulting in a larger contact area and a higher elastic interaction strength.

IV Conclusion

We investigated the viscoelastic response of assembled patchy particles. By decomposing spontaneous bending fluctuations into bending modes, we found that patchy particle chains are well described by semiflexible filaments with a persistence length set by the patch size and the temperature-dependent strength of the critical Casimir interaction. Further dynamical analysis revealed rich viscoelastic behavior, in which the bending fluctuations follow a two-step relaxation process similar to that of biopolymers: a fast elastic relaxation, followed by a slower non-elastic one. We attribute the latter to a combination of external friction due to drag and internal friction due to contact mechanics of the bonding patches. Internal friction effects have also been observed for microtubules;^{44,45,54–56} while their fast relaxation is of the same damped elastic nature as for our colloidal chain, however, the internal friction is of different microscopic origin: in microtubules, it has been associated with solvent drainage through the porous structure. In our quasi two-dimensional case of single polymers, these effects are not relevant, and we associate the internal friction with contact mechanics of the patches. Nevertheless, the presence of such internal friction in our colloidal model system suggests that these type of effects may be general and could be expected in other filaments that consist of segmented units, such as nanoparticle chains.⁵⁷

These results, while still in two dimensions, open the door to the rational design of colloidal architectures with programmed viscoelastic properties. For example, by implementing higher-valency particles serving as branching points, one can make three-dimensional equilibrium networks^{29,58,59} or cyclic structures mimicking cyclic molecular structures.⁶⁰ Our system can then be extended into three dimensions by density matching the binary solvent *via* the addition of sucrose

that, as preliminary results show, does not affect the solvent phase diagram. The design parameters to control the mechanics of these structures are then the properties of the particle patches (angle and surface friction) and their interactions, in our case set by the critical Casimir force. The latter can not only be used to control the radial interaction strength, but also the shear rigidity between bonded colloids. Our results encourage investigation of the effect of bending rigidity in general colloidal molecules and networks, whose structure and rheology are expected to have a non-trivial dependence on rigidity. In this case, the bending rigidity will be a crucial factor determining the structural stability; its *in situ* control could yield switchable mechanical states and shape changing behavior.^{61,62} Further opportunities arise for the study of dense semiflexible polymers, for which the colloidal analogue can provide visualization of polymer interactions and their effects on the kinetics.³¹ Finally, opportunities arise for the assembly of nanoparticles such as quantum dots into materials, where besides mechanical properties, optical and electrical properties come into play^{63–65} that are dependent on the assembled structure.

Conflicts of interest

There are no conflicts to declare.

Acknowledgements

We thank Michele Zanini for the AFM data and analysis. P. S. acknowledges support by Vici fellowship 680-47-615 from the Netherlands Organization for Scientific Research (NWO). H. J. J., P. G. B and P. S. acknowledge support by grant 680.91.124 from NWO.

References

- M. R. Wasserman and S. Liu, *Biochemistry*, 2019, **58**, 4667–4676.
- C. P. Lowe, *Philos. Trans. R. Soc., B*, 2003, **358**, 1543–1550.
- T. S. Yu, E. Lauga and A. E. Hosoi, *Phys. Fluids*, 2006, **18**, 091701.
- E. Lauga and T. R. Powers, *Rep. Prog. Phys.*, 2009, **72**, 096601.
- C. P. Broedersz and F. C. MacKintosh, *Rev. Mod. Phys.*, 2014, **86**, 995–1036.
- C. P. Broedersz, X. Mao, T. C. Lubensky and F. C. MacKintosh, *Nat. Phys.*, 2011, **7**, 983–988.
- C. Schuldt, J. Schnauß, T. Handler, M. Glaser, J. Lorenz, T. Golde, J. A. Käs and D. M. Smith, *Phys. Rev. Lett.*, 2016, **117**, 197801.
- R. Rens and E. Lerner, *Eur. Phys. J. E*, 2019, **42**, 114.
- J. M. van Doorn, J. E. Verweij, J. Sprakel and J. van der Gucht, *Phys. Rev. Lett.*, 2018, **120**, 208005.
- D. C. Morse, *Macromolecules*, 1998, **31**, 7030–7067.
- I. Kirchenbuechler, D. Guu, N. A. Kurniawan, G. H. Koenderink and M. P. Lettinga, *Nat. Commun.*, 2014, **5**, 5060.
- L. Feng, L.-L. Pontani, R. Dreyfus, P. Chaikin and J. Brujic, *Soft Matter*, 2013, **9**, 9816–9823.
- B. Biswas, R. K. Manna, A. Laskar, P. B. S. Kumar, R. Adhikari and G. Kumaraswamy, *ACS Nano*, 2017, **11**, 10025–10031.
- D. Nishiguchi, J. Iwasawa, H.-R. Jiang and M. Sano, *New J. Phys.*, 2018, **20**, 015002.
- A. D. Dinsmore, V. Prasad, I. Y. Wong and D. A. Weitz, *Phys. Rev. Lett.*, 2006, **96**, 185502.
- J. P. Pantina and E. M. Furst, *Phys. Rev. Lett.*, 2005, **94**, 138301.
- S. G. Stuij, J. M. van Doorn, T. Kodger, J. Sprakel, C. Coulaix and P. Schall, *Phys. Rev. Res.*, 2019, **1**, 023033.
- Z. Gong, T. Hueckel, G. R. Yi and S. Sacanna, *Nature*, 2017, **550**, 234–238.
- W. B. Rogers, W. M. Shih and V. N. Manoharan, *Nat. Rev. Mater.*, 2016, **1**, 16008.
- D. J. Kraft, R. Ni, F. Smalenburg, M. Hermes, K. Yoon, D. A. Weitz, A. van Blaaderen, J. Groenewold, M. Dijkstra and W. K. Kegel, *Proc. Natl. Acad. Sci. U. S. A.*, 2012, **109**, 10787–10792.
- J. R. Wolters, G. Avisati, F. Hagemans, T. Vissers, D. J. Kraft, M. Dijkstra and W. K. Kegel, *Soft Matter*, 2015, **11**, 1067–1077.
- C. H. J. Evers, J. A. Luiken, P. G. Bolhuis and W. K. Kegel, *Nature*, 2016, **534**, 364.
- S. Sacanna, W. T. M. Irvine, P. M. Chaikin and D. J. Pine, *Nature*, 2010, **464**, 575.
- A. McMullen, M. Holmes-Cerfon, F. Sciortino, A. Y. Grosberg and J. Brujic, *Phys. Rev. Lett.*, 2018, **121**, 138002.
- M. Y. Ben Zion, X. He, C. C. Maass, R. Sha, N. C. Seeman and P. M. Chaikin, *Science*, 2017, **358**, 633–636.
- A. A. Shah, B. Schultz, W. Zhang, S. C. Glotzer and M. J. Solomon, *Nat. Mater.*, 2014, **14**, 117.
- J. Yan, M. Han, J. Zhang, C. Xu, E. Luijten and S. Granick, *Nat. Mater.*, 2016, **15**, 1095–1100.
- F. Sciortino, E. Bianchi, J. F. Douglas and P. Tartaglia, *J. Chem. Phys.*, 2007, **126**, 194903.
- E. Bianchi, B. Capone, I. Coluzza, L. Rovigatti and P. D. J. van Oostrum, *Phys. Chem. Chem. Phys.*, 2017, **19**, 19847–19868.
- T. A. Nguyen, A. Newton, S. J. Veen, D. J. Kraft, P. G. Bolhuis and P. Schall, *Adv. Mater.*, 2017, **29**, 1–6.
- S. G. Stuij, J. Rouwhorst, H. J. Jonas, N. Rufino, Z. Gong, S. Sacanna, P. G. Bolhuis and P. Schall, arXiv preprint, 2021, arXiv:2106.04346.
- C. Hertlein, L. Helden, A. Gambassi, S. Dietrich and C. Bechinger, *Nature*, 2008, **451**, 172.
- A. Gambassi, A. Maciołek, C. Hertlein, U. Nellen, L. Helden, C. Bechinger and S. Dietrich, *Phys. Rev. E: Stat., Nonlinear, Soft Matter Phys.*, 2009, **80**, 061143.
- U. Nellen, L. Helden and C. Bechinger, *EPL*, 2009, **88**, 26001.
- M. Tröndle, S. Kondrat, A. Gambassi, L. Harnau and S. Dietrich, *J. Chem. Phys.*, 2010, **133**, 074702.
- T. F. Mohry, A. Maciołek and S. Dietrich, *J. Chem. Phys.*, 2012, **136**, 224902.
- S. G. Stuij, M. Labbé-Laurent, T. Kodger, A. Maciołek and P. Schall, *Soft Matter*, 2017, **13**, 5233–5249.
- V. D. Nguyen, S. Faber, Z. Hu, G. H. Wegdam and P. Schall, *Nat. Commun.*, 2013, **4**, 1584.

- 39 M. T. Dang, A. V. Verde, V. D. Nguyen, P. G. Bolhuis and P. Schall, *J. Chem. Phys.*, 2013, **139**, 094903.
- 40 V. D. Nguyen, M. T. Dang, T. A. Nguyen and P. Schall, *J. Phys.: Condens. Matter*, 2016, **28**, 043001.
- 41 S. Veen, M. Potenza, M. Alaimo, O. Antoniuk, S. Mazzoni, P. Schall and G. Wegdam, *Phys. Rev. Lett.*, 2012, **109**, 248302.
- 42 P. Shelke, D. Nguyen, A. V. Limaye and P. Schall, *Adv. Mater.*, 2013, **25**, 1499.
- 43 J. Rouwhorst, C. Ness, A. Zaccone and P. Schall, *Nat. Commun.*, 2021, **11**, 3558.
- 44 M. G. Poirier and J. F. Marko, *Phys. Rev. Lett.*, 2002, **88**, 228103.
- 45 C. P. Brangwynne, G. H. Koenderink, E. Barry, Z. Dogic, F. C. MacKintosh and D. A. Weitz, *Biophys. J.*, 2007, **93**, 346–359.
- 46 G. A. Buxton and N. Clarke, *Phys. Rev. Lett.*, 2007, **98**, 238103.
- 47 X. Mao, N. Xu and T. C. Lubensky, *Phys. Rev. Lett.*, 2010, **104**, 085504.
- 48 Q. Wu, J. van der Gucht and T. E. Kodger, *Phys. Rev. Lett.*, 2020, **125**, 208004.
- 49 D. Allan, T. Caswell, N. Keim and C. van der Wel, *trackpy: Trackpy v0.3.1*, 2016.
- 50 M. D. Carbajal-Tinoco, R. Lopez-Fernandez and J. L. Arauz-Lara, *Phys. Rev. Lett.*, 2007, **99**, 138303.
- 51 A. Stein, S. J. Davidson, J. C. Allegra and G. F. Allen, *J. Chem. Phys.*, 1972, **56**, 6164–6168.
- 52 D. Nykypanchuk, M. M. Maye, D. van der Lelie and O. Gang, *Langmuir*, 2007, **23**, 6305–6314.
- 53 D. Li, S. Banon and S. L. Biswal, *Soft Matter*, 2010, **6**, 4197–4204.
- 54 A. Maghsoodi and N. Perkins, *Sci. Rep.*, 2018, **8**, 11684.
- 55 K. M. Taute, F. Pampaloni, E. Frey and E.-L. Florin, *Phys. Rev. Lett.*, 2008, **100**, 028102.
- 56 T. Hiraiwa and T. Ohta, *J. Chem. Phys.*, 2010, **133**, 044907.
- 57 K. Liu, Z. Nie, N. Zhao, W. Li, M. Rubinstein and E. Kumacheva, *Science*, 2010, **329**, 197–200.
- 58 F. Sciortino and E. Zaccarelli, *Curr. Opin. Solid State Mater. Sci.*, 2011, **15**, 246–253.
- 59 F. Smallenburg and F. Sciortino, *Nat. Phys.*, 2013, **9**, 554.
- 60 P. J. M. Swinkels, S. G. Stuij, Z. Gong, H. Jonas, B. van der Linden, P. G. Bolhuis, S. Sacanna, S. Woutersen and P. Schall, *Nat. Commun.*, 2021, **12**, 2810.
- 61 K. Bertoldi, V. Vitelli, J. Christensen and M. van Hecke, *Nat. Rev. Mater.*, 2017, **2**, 17066.
- 62 M. Z. Miskin, K. J. Dorsey, B. Bircan, Y. Han, D. A. Muller, P. L. McEuen and I. Cohen, *Proc. Natl. Acad. Sci. U. S. A.*, 2018, **115**, 466–470.
- 63 E. Marino, D. M. Balazs, R. W. Crisp, D. Hermida-Merino, M. A. Loi, T. E. Kodger and P. Schall, *J. Phys. Chem. C*, 2021, **123**, 13451–13457.
- 64 E. Marino, A. Sciortino, A. Berkhout, K. E. MacArthur, M. Heggen, T. Gregorkiewicz, T. E. Kodger, A. Capretti, C. Murray, F. Koenderink, F. Messina and P. Schall, *ACS Nano*, 2020, **14**, 13806.
- 65 E. Marino, O. A. Vasilyev, B. B. Kluft, M. J. B. Stroink, S. Kondrat and P. Schall, *Nanoscale Horiz.*, 2021, DOI: 10.1039/D0NH00670J.